

Available online at [www.sciencedirect.com](http://www.sciencedirect.com)**ScienceDirect**journal homepage: [www.elsevier.com/locate/he](http://www.elsevier.com/locate/he)

# Impedance of a tubular electrochemical cell with BZCY electrolyte and Ni-BZCY cermet electrodes for proton ceramic membrane reactors

Irene Yuste-Tirados <sup>a,b</sup>, Xin Liu <sup>a,b</sup>, Christian Kjølseth <sup>b,\*</sup>, Truls Norby <sup>a,\*\*</sup><sup>a</sup> Centre for Materials Science and Nanotechnology, Department of Chemistry, University of Oslo, Gaustadalléen 21, NO-0349, Oslo, Norway<sup>b</sup> CoorsTek Membrane Sciences AS, Gaustadalléen 21, NO-0349, Oslo, Norway

## HIGHLIGHTS

- Impedance spectroscopy on a complete proton ceramic tubular cell with asymmetric Ni-BCZY cermet electrodes.
- Differentiates electrode contributions and identifies polarisation mechanisms.
- Hydrogen gas diffusion limitation in the thick cermet dominates total polarisation under applied conditions.

## ARTICLE INFO

### Article history:

Received 19 February 2023

Received in revised form

23 March 2023

Accepted 25 March 2023

Available online 2 May 2023

### Keywords:

Proton ceramic electrochemical cell

Electrode reaction mechanism

Impedance spectroscopy

Hydrogen separation

## ABSTRACT

In this work, impedance spectroscopy has been employed to explore the electrochemical behaviour of a  $15\text{ cm}^2$  complete tubular cell with  $\text{BaZr}_{0.8}\text{Ce}_{0.1}\text{Y}_{0.1}\text{O}_{3-\delta}$  (BZCY) electrolyte and two asymmetric Ni-BCZY cermet electrodes for hydrogen separation. Analyses of impedance spectra at different temperatures and gas compositions reveal that the thick inner electrode contributes most to the total polarisation resistance ( $R_p$ ). For  $R_p$  there are four contributions with well-separated time constants of which gas phase hydrogen diffusion within the porous Ni-BZCY anode is predominant. The other three can be ascribed to proton migration through the space charge layer of the BZCY electrolyte adjacent to the Ni electrode, hydrogen redox charge transfer reactions, and hydrogen diffusion within Ni bulk. The present study guides the way to parameterise and, on this basis, optimise electrodes for scalable proton ceramic electrochemical cells.

© 2023 The Author(s). Published by Elsevier Ltd on behalf of Hydrogen Energy Publications LLC. This is an open access article under the CC BY license (<http://creativecommons.org/licenses/by/4.0/>).

## Introduction

Hydrogen as a clean and inexhaustible energy carrier will play an important role in the transition toward a net-zero carbon society. Electrochemical cells can convert renewable

electricity to hydrogen gas in a single step, providing an efficient way to balance energy generation and demand. Proton ceramic electrochemical cell (PCECs) are of interest with potential for relatively low material cost and high electrochemical efficiency [1–6]. Compared with the oxide-ion conducting counterparts, PCECs operate at moderate

\* Corresponding author.

\*\* Corresponding author.

E-mail addresses: [i.t.yuste@smn.uio.no](mailto:i.t.yuste@smn.uio.no) (I. Yuste-Tirados), [xinliu@smn.uio.no](mailto:xinliu@smn.uio.no) (X. Liu), [ckjolseth@CoorsTek.com](mailto:ckjolseth@CoorsTek.com) (C. Kjølseth), [truls.norby@kjemi.uio.no](mailto:truls.norby@kjemi.uio.no) (T. Norby).

<https://doi.org/10.1016/j.ijhydene.2023.03.401>

0360-3199/© 2023 The Author(s). Published by Elsevier Ltd on behalf of Hydrogen Energy Publications LLC. This is an open access article under the CC BY license (<http://creativecommons.org/licenses/by/4.0/>).

temperatures 500–700 °C, with potential for better longevity and smaller balance-of-plant [7–9]. To date, solid solutions of BaZrO<sub>3</sub> and BaCeO<sub>3</sub> doped with acceptors such as Y<sub>2</sub>O<sub>3</sub> (BZCY) are considered as the state-of-the-art proton-conducting electrolyte materials for PCECs [10–12].

Hydrogen production or separation utilising PCECs [1–3,13,14] comprise extraction of hydrogen from the feedstock dehydrogenation reactions (e.g., hydrocarbons or ammonia) in the form of protons in the electrolyte and electrons in the anode, migration, and recombination of protons and electrons into hydrogen at the cathode. These processes and their mechanistic steps impose different contributions to electrical and chemical polarisation (seen as resistances) of cell, which determines power consumption and energy efficiency. A fundamental understanding and parameterisation of these processes together with underlying mechanisms is of vital importance to enhance cell performance.

Electrochemical impedance spectroscopy (EIS) has been widely employed to study mechanisms and kinetics of Ni-BZCY electrode reactions [15–22]. Most previous reports have focused on a single Ni-BCZY electrode using either three-electrode or symmetrical (in a single chamber) two-electrode cells [23–26]. The three-electrode configuration is scientifically most proper but cannot be applied to thin electrolytes and hence hardly realistic high drain processes. The symmetric two-electrode configuration is convenient for high-frequency EIS under open circuit conditions, but DC and probably also low-frequency AC currents add anodic and cathodic polarisation in a way that is challenging both for fitting individual impedance spectra and for identifying the polarisation processes that are involved. Inputs to the puzzle is typically sought overcome by recording impedance spectra under different conditions, e.g., temperature and gas composition [21]. Impedance responses of the two electrodes typically overlap, but not completely, adding to the difficulty of identifying individual polarisations [27,28]. In this work, we apply impedance spectroscopy to tubular cells with thin BaZr<sub>0.8</sub>Ce<sub>0.1</sub>Y<sub>0.1</sub>O<sub>3-δ</sub> (BZCY81) electrolytes and two Ni–BaZr<sub>0.7</sub>Ce<sub>0.2</sub>Y<sub>0.1</sub>O<sub>3-δ</sub> (Ni-BZCY72) electrodes with different thicknesses and microstructure in two different gas chambers (Fig. 1) for hydrogen separation. By varying the gas compositions individually on the two electrodes with different

microstructures, it enables us to differentiate their separate contributions to the polarisation resistances and identify polarisation mechanisms with greater certainty than in literature so far. The cells used here are designed to operate under high DC current load, and this work forms a fundament for further studies with modelling, parameterisation, and optimisation of complete cells in operation.

## Experimental

### Fabrication of ceramic tubular cells

The tubular PCEC cell comprises a dense 25–30 μm thick BaZr<sub>0.8</sub>Ce<sub>0.1</sub>Y<sub>0.1</sub>O<sub>3-δ</sub> (BZCY81) proton conducting electrolyte between Ni-BZCY cermet cylindrical electrodes of thickness 700 μm (inner, supporting) and 10 μm (outer, coated). These tubular membrane cells were produced at CoorsTek Membrane Sciences AS (Oslo, Norway) by co-sintering of a coated, extruded substrate. The extrudate consisted of a mixture of ceramic powders, an aqueous binder system of methylcellulose (Methocel E10 M, DuPont), starch (Redisol, Tate & Lyle), and polyethylene glycol as rheology modifier (PEG400, Sigma Aldrich). The ceramic component of the extrudate was a blend of 60 wt % NiO (IP Grade, Sumitomo) and 40 wt% of a precursor powder mixture of BaSO<sub>4</sub> (Blanc Fixe N, Solvay), CeO<sub>2</sub> (CE-OX-O3, American Elements), ZrO<sub>2</sub> (AMR), and Y<sub>2</sub>O<sub>3</sub> (HJD International), in molar ratios to yield BaZr<sub>0.7</sub>Ce<sub>0.2</sub>Y<sub>0.1</sub>O<sub>3-δ</sub> (BZCY72) on decomposition and reaction. The precursor powders were first milled to a nominal particle size of 0.3 μm, while NiO was used as received with a particle size of 1 μm.

After extrusion and drying, the green substrate was coated with a slurry consisting of the precursors, methyl methacrylate binder (Elvacite 2927, Mitsubishi Chemical), pentyl acetate organic solvent (Sigma Aldrich) and terpineol as a rheological additive (Sigma Aldrich) using an automated spray-coater (Max-800, Ultrasonic Systems). The stoichiometry of the precursors used for the coating was adjusted to produce BZCY81. The outer electrode, also made of NI-BZCY, was applied by dip-coating the two-layered green tube in a slurry containing a mixture of 40–50 wt% ceramic powders and the aqueous binder system. The composition of the powder mixture was

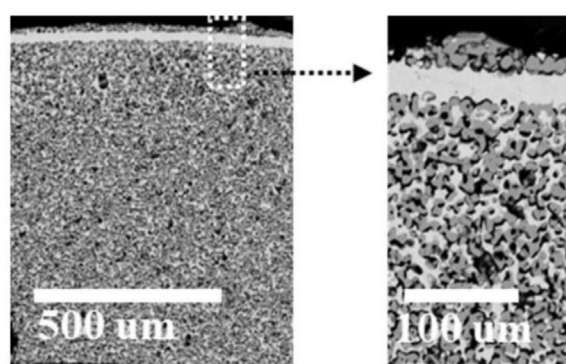
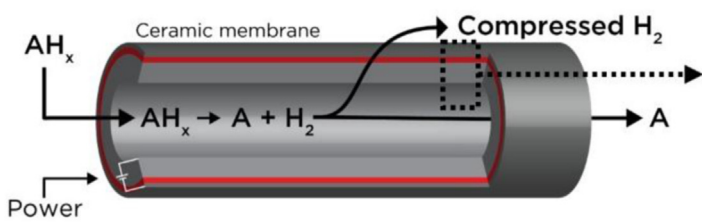


**Fig. 1 – Left,** schematic of the tubular cell used in this work where hydrogen is extracted from the inside and transferred to the outside; **SEM micrograph** of the cross-section with this BZCY electrolyte and two composite Ni-BZCY electrodes, the inner thick (supporting) and the outer thin (coated). **SEM micrograph** of a zoom in into the interphases area of the cross section.

otherwise identical to that used to fabricate the substrate. The three-layered green ceramic tubes were then sintered at 1610 °C for 15 h to full density in a muffle furnace. Subsequent reduction of the NiO component of the electrodes was done at 1000 °C for 24 h in a flow of 5% H<sub>2</sub> balanced with Ar. This resulted in an anode support with an open porosity of 26 vol.% as measured using the Archimedes method and corroborated with area analysis of polished cross sectioned samples. The dense electrolyte membrane thickness was 25–30 μm [1,4,29].

### Electrical measurements

The tubular cell was mounted in a ProboStat™ sample holder (NorECs, Norway) providing feedthroughs of electrical contacts and gases (Fig. 2). A Pt–Pt10Rh thermocouple was placed in the tube enclosing the outer chamber. Two wires supported on an alumina tube (O.D. = 5 mm) was inserted into the tubular cell as current collector and voltage probe. Ni wool (American Elements) was inserted to ensure good contact between the inner electrode and the electrical feedthroughs. For outer current collection and outer voltage probe, Cu wire (Good-Fellow Cu-OFHC, 0.25 mm) was braided around the tube and connected to the electrical feedthroughs of the ProboStat™. The heated part of the ProboStat™ was placed in a furnace of the test rig. The gas flows and compositions were controlled by calibrated mass flow controllers (red-y, Vögtlin Instruments).

EIS was performed to evaluate the polarisation behaviour of the tubular ceramic cells using a Gamry Reference 3000™ potentiostat/galvanostat/Zero Resistance Ammeter. The frequency range used was from 1 MHz to 0.01 Hz with signal amplitude 50 mA rms. Measurements were performed at 50 °C intervals in the temperature range from 600 to 750 °C. Hydrogen partial pressure (pH<sub>2</sub>) was only varied in one of the chambers, for instance, in the inner chamber while keeping pH<sub>2</sub> of the outer chamber constant, and vice versa. Impedance spectra were recorded after 1 h at each specific condition to

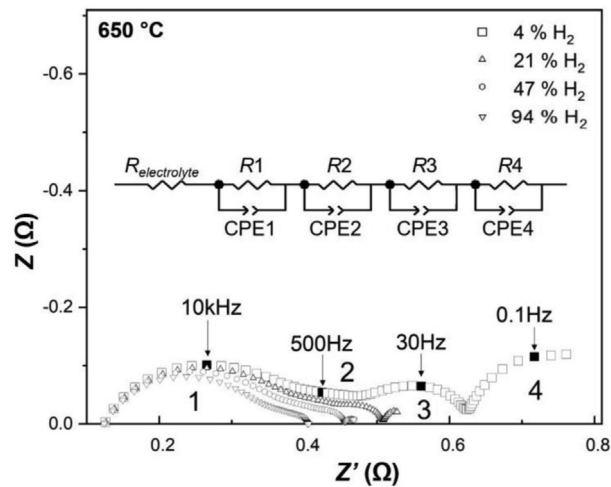


**Fig. 3 – EIS spectra of a tubular cell with Ni-BCZY symmetric electrodes and BZCY electrolyte measured at 650 °C with different H<sub>2</sub> contents in the H<sub>2</sub> and Ar atmosphere at both electrodes.**

ensure equilibrated conditions. Humidification was obtained by bubbling gases through water at room temperature, producing approximately 3% (vol.) water in the gas. The impedance spectra were fitted using the software ZView (Scribner Associates).

## Results

### Electrochemical impedance spectroscopy

Typical Nyquist plots show four resolvable arcs (Fig. 3) and was analysed by an equivalent circuit (inset in Fig. 3) that

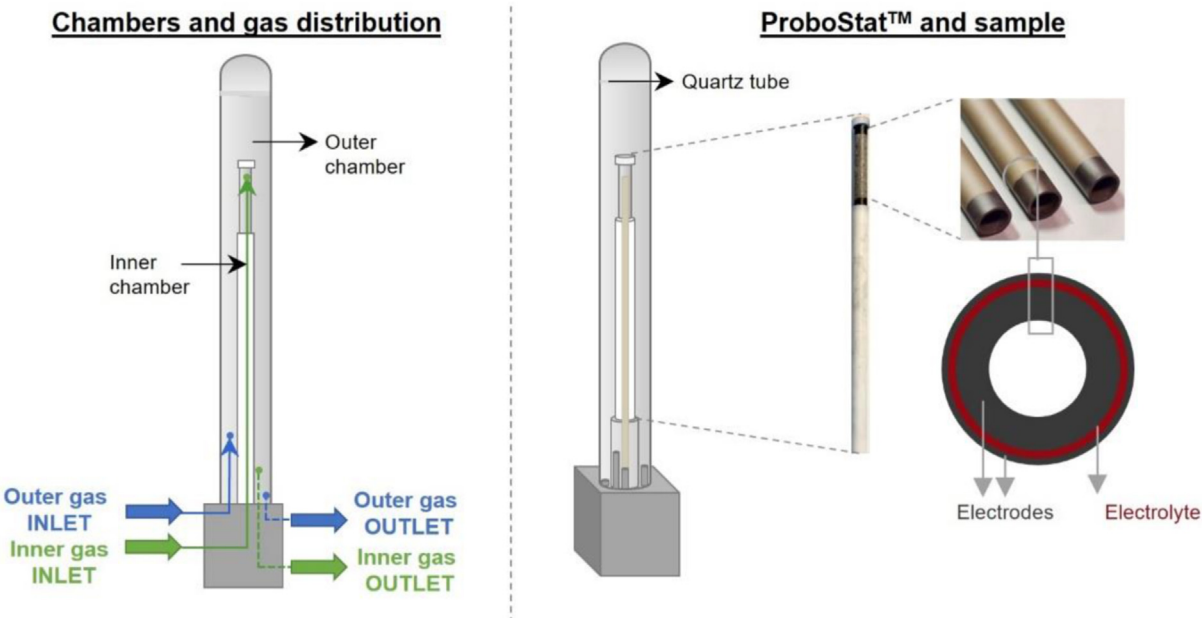


**Fig. 2 – Description of the measurement set-up for a 5 cm long tubular sample with total active area of 14.8 cm<sup>2</sup>.**

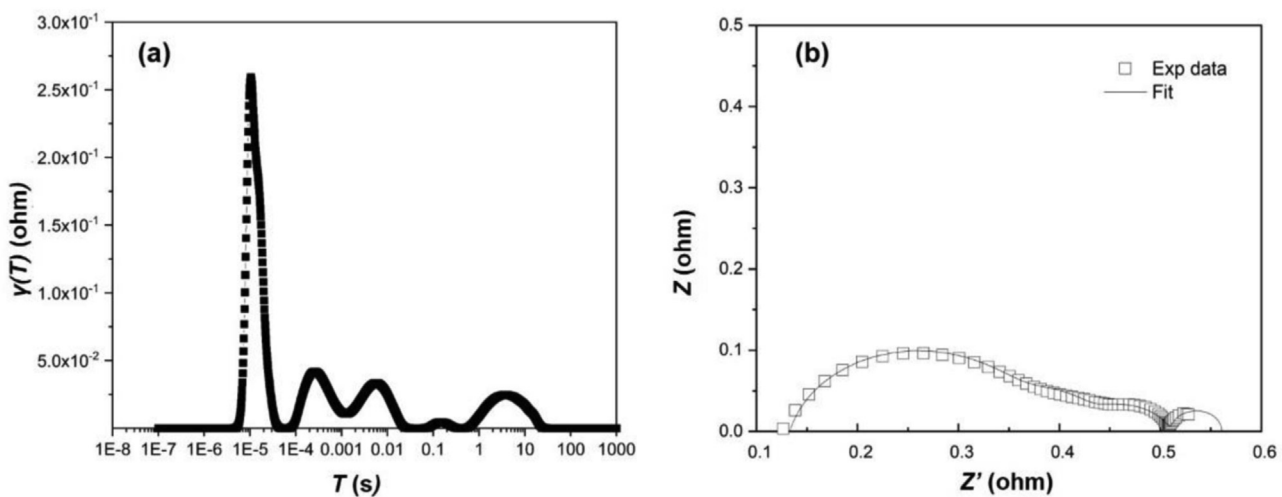


Fig. 4 – (a). DRT function with Gaussian discretization and a discretization factor of 0.009 calculated from impedance spectra of a tubular cell with two Ni-BZCY electrodes and BZCY electrolyte measured at 650 °C with  $pH_2 = 0.2$  bar in the inner chamber and 0.05 bar in the outer chamber. (b). Comparison of experimental impedance spectrum and modelled fit for same impedance spectra as in A.

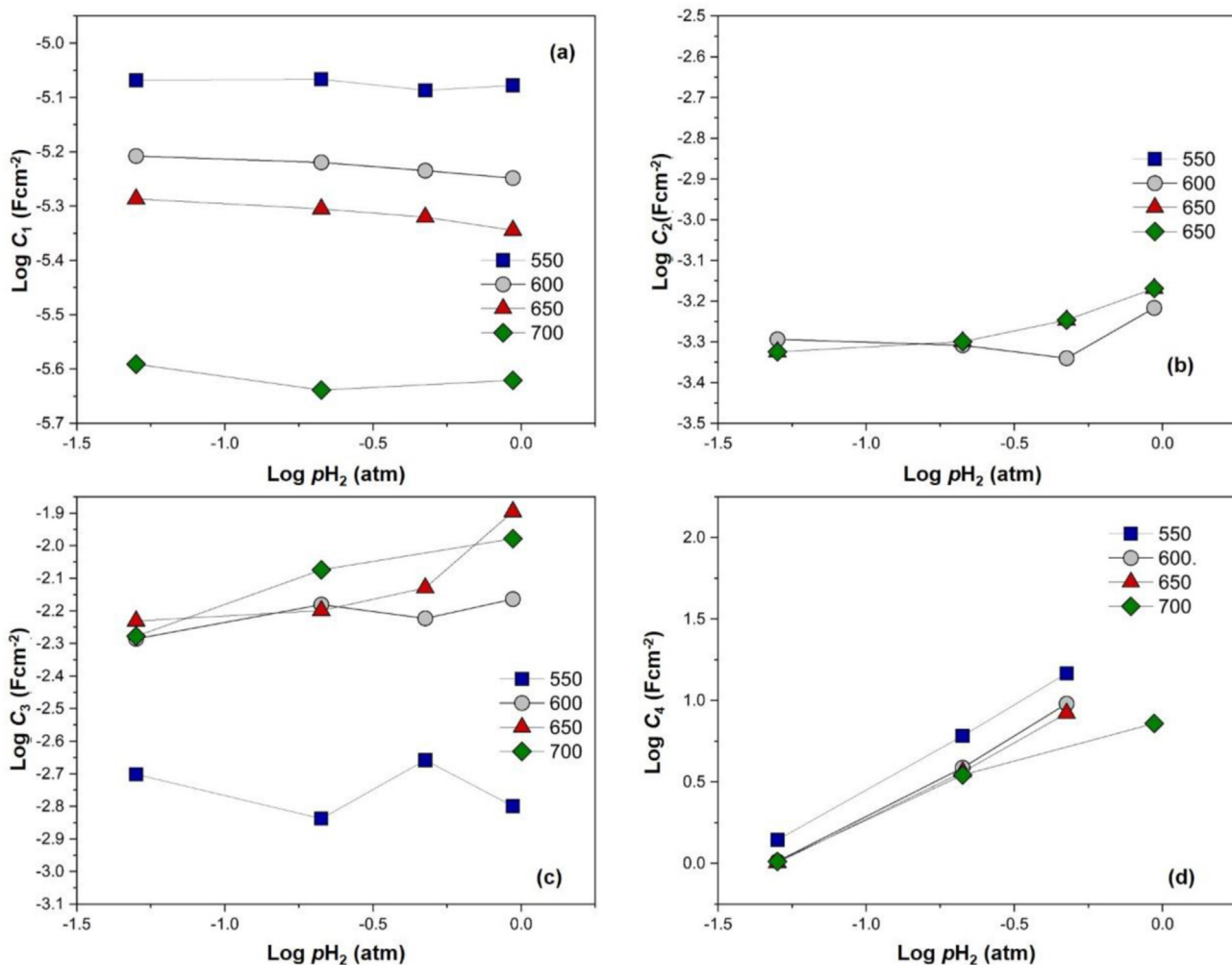


Fig. 5 – Capacitances as a function of  $pH_2$  and temperature for Ni-BZCY/BZCY/Ni-BZCY tubular cells in an open chamber configuration ( $pH_2$  for both inside and outside).

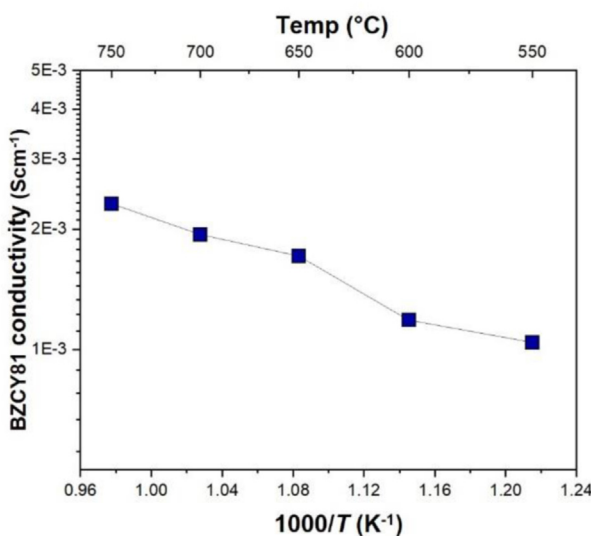


Fig. 6 – Protionic conductivity of BZCY81 electrolyte as a function of temperature in wet H<sub>2</sub>.

describes the characteristics of four steps of the electrochemical processes. These four steps have also been consistent with a distribution of relaxation times (DRT) analysis as shown in Fig. 4a. The equivalent circuit consists of a series connection with a resistor,  $R_{\text{electrolyte}}$  (representing the electrolyte ohmic resistance) followed by four RQ elements. The RQ elements can be fitted to arcs (depressed semicircles), from which the extracted parameters are the resistance,  $R$ , the pseudo-capacitance,  $Q$ , and the parameter  $n$  that together relate to the representative capacitance  $C$  by the equation:

$$C = R^{\frac{(1-n)}{n}} (Y_0 \cdot \omega^n)^{\frac{1}{n}} \quad (1)$$

where  $\omega = 2\pi f$  is the angular frequency. In Fig. 4b, an example is presented wherein the experimental data is fitted to the described equivalent circuit.

The pseudo-capacitance values of the responses for both electrodes are calculated to be  $C_1 \approx 5 \cdot 10^{-6} \text{ F cm}^{-2}$ ,  $C_2 \approx 5 \cdot 10^{-4} \text{ F cm}^{-2}$ ,  $C_3 \approx 2 - 5 \cdot 10^{-3} \text{ F cm}^{-2}$ , and  $C_4 \approx 2 \text{ F cm}^{-2}$  (Fig. 5), in agreement with a previous report on tubular cells with Ni-BZCY electrodes [2]. Based on their well-separated time constants, the four arcs represent distinct electrode

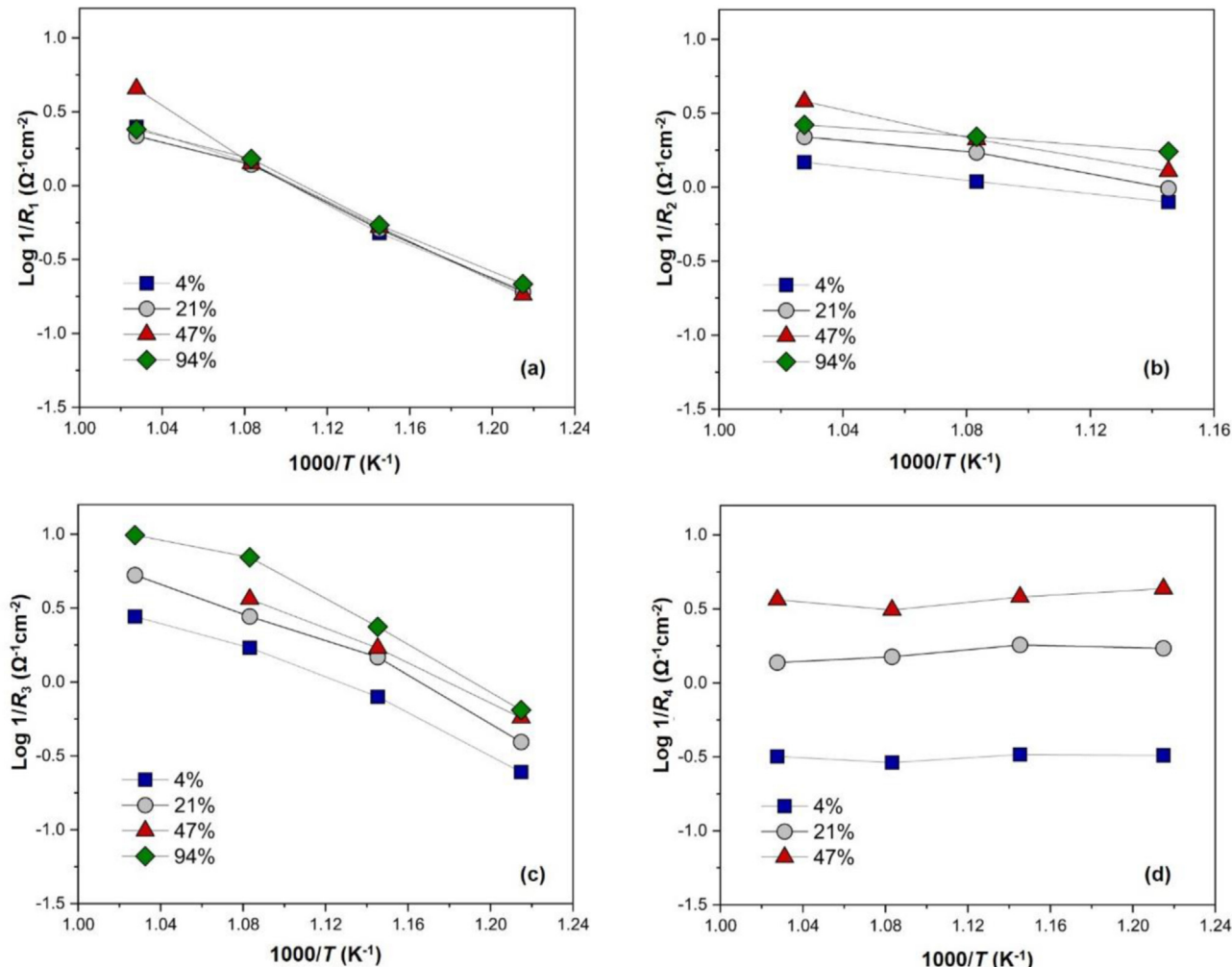
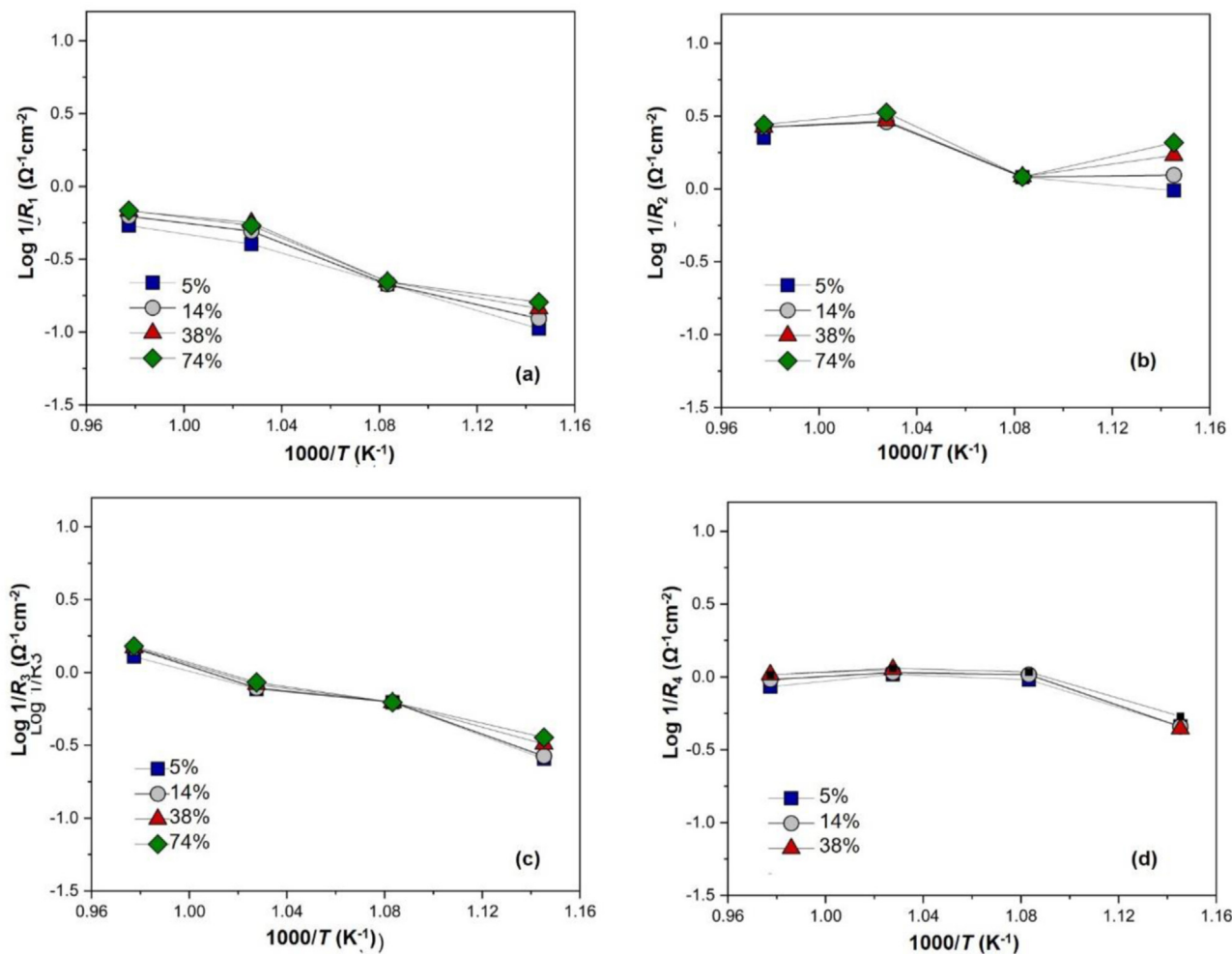


Fig. 7 – Temperature dependency of (a) 1/R<sub>1</sub>, (b) 1/R<sub>2</sub>, (c) 1/R<sub>3</sub>, (d) 1/R<sub>4</sub>. Measurement conditions: temperature range from 550 to 700 °C, pH<sub>2</sub> in the inner chamber varies from 4% to 94% H<sub>2</sub> and pH<sub>2</sub> in the outer chamber is 5%.



**Fig. 8 – Temperature dependency of (a)  $1/R_1$ , (b)  $1/R_2$  (c)  $1/R_3$  (d)  $1/R_4$ . Measurement conditions: temperature range from 550 to 700 °C,  $pH_2$  in the outer chamber varies from 4% to 94% H<sub>2</sub> and  $pH_2$  in the inner chamber is set to be 5%.**

responses [24,25], and the parameter  $n$  is calculated to be 0.75, 0.70, 0.85, and 1 for  $n_1$ ,  $n_2$ ,  $n_3$ , and  $n_4$ , respectively. From Fig. 5,  $C_1$  –  $C_3$  appear to be independent of  $pH_2$ , while  $C_4$  increases with increasing  $pH_2$ .

The protonic conductivity of the BZCY81 electrolyte, calculated from  $R_{\text{electrolyte}}$ , is plotted as a function of temperature in Fig. 6. The conductivity values are of the order of  $10^{-3}$  S cm<sup>-1</sup> in the range of 550–750 °C, with an activation energy of 0.39 eV calculated from  $\sigma T$  plots, being close to the literature values [24,25].

The polarisation resistances as a function of temperature and  $pH_2$  (only varied in the inner chamber) are plotted in Fig. 7. The activation energies of total polarisation resistance are calculated in the range of 0.44–0.82 eV, in good agreement with previous reports on Ni cermet electrodes of PCECs [2,30–32].

For the electrode polarisation resistances  $R_1$  the activation energies are calculated to be around 1.18 eV, seemingly independent of  $pH_2$ . In contrast, the activation energies of  $R_2$  show a clear  $pH_2$  dependency and vary from 0.3 to 0.7 eV. For  $R_3$ , the activation energies are around 1.24 eV. In contrast, the values of  $R_4$  do not show any temperature dependency.

Similar experiments have been performed by varying  $pH_2$  in the outer chamber, as shown in Fig. 8. There is nearly no change, neither in thermal activation nor pre-exponentials, indicating that the polarisation resistance of our tubular cells is dominated by the thick inner Ni-BZCY electrode under the applied conditions.

Fig. 9 shows the dependency of each polarisation resistance on  $pH_2$  in the inner chamber, while keeping  $pH_2$  in the outer chamber constant at 0.05 bar. The  $1/R_1$  is close to independent of  $pH_2$  for all temperatures, while  $1/R_2$  shows a slight  $pH_2$  dependence with  $1/R_2 \propto pH_2^{0.21}$ . In contrast, the low frequency ones, i.e.,  $1/R_3$  and  $1/R_4$ , show a higher sensitivity to  $pH_2$  in the inner chamber, exhibiting  $pH_2$  dependences of approximately  $1/R_3 \propto pH_2^{0.38}$  and  $1/R_4 \propto pH_2^{1.04}$ , respectively.

Fig. 10 shows dependences of each polarisation resistance on  $pH_2$  in the outer chamber, while keeping  $pH_2$  in the inner chamber constant at 0.06 bar.  $1/R_1$ ,  $1/R_3$ , and  $1/R_4$  do not show any  $pH_2$  dependency in the temperature range from 650 to 750 °C, but a vague  $pH_2$  dependency was observed at 600 °C. The  $1/R_2$  exhibit a  $pH_2$  dependence around  $1/R_2 \propto pH_2^{0.15}$ .

## Discussion

### Proposed reaction mechanism

**Fig. 11** schematically illustrates the interface between electrode and electrolyte together with potential reaction paths. As both electrodes have the same composition and the cell is operating as a hydrogen pump, the electrochemical reactions and processes should be identical for both electrodes but in opposite direction and order (**Fig. 11** and **Table 1**).

The proposed reaction mechanism in the anodic direction firstly involves gas phase H<sub>2</sub> diffusion, followed with dissociative H<sub>2</sub> chemisorption to form atomic hydrogen (H) on the Ni surface [33]. Subsequently, H atoms can diffuse on the Ni surface and/or through the Ni bulk to reach the two-phase boundary area (2 PB). Here, we will have charge transfer to form a proton in the electrolyte and leave an electron in the Ni [34]. The protons migrate through the space charge boundary region of the electrolyte-electrode interface and then enter the

bulk of the BZCY electrolyte. Electrons are collected in the electrode to the external circuit.

Importantly, we postulate that H diffuses on and in Ni and hence utilises more or less of the 2 PB in proportion to what gives the lowest overall impedance and polarisation. If chemisorption is slow, the process needs a lot of surface and hence surface diffusion. If the charge transfer or transport through the space charge layer or electrolyte is slow, it needs diffusion through bulk and access to a lot of 2 PB area. The surface diffusion all the way to the 3 PB line often presented as a separate path is simply an extreme of our more complete description.

### High frequency electrode response

The 1/R<sub>1</sub> shows a weak dependence on pH<sub>2</sub> in both inner and outer chamber and a relatively high activation energy of 1.18 eV. Previous works on oxide-ion conducting SOFC cermet electrodes has ascribed this high frequency process to an electrolyte grain boundary response [35]. However, grain

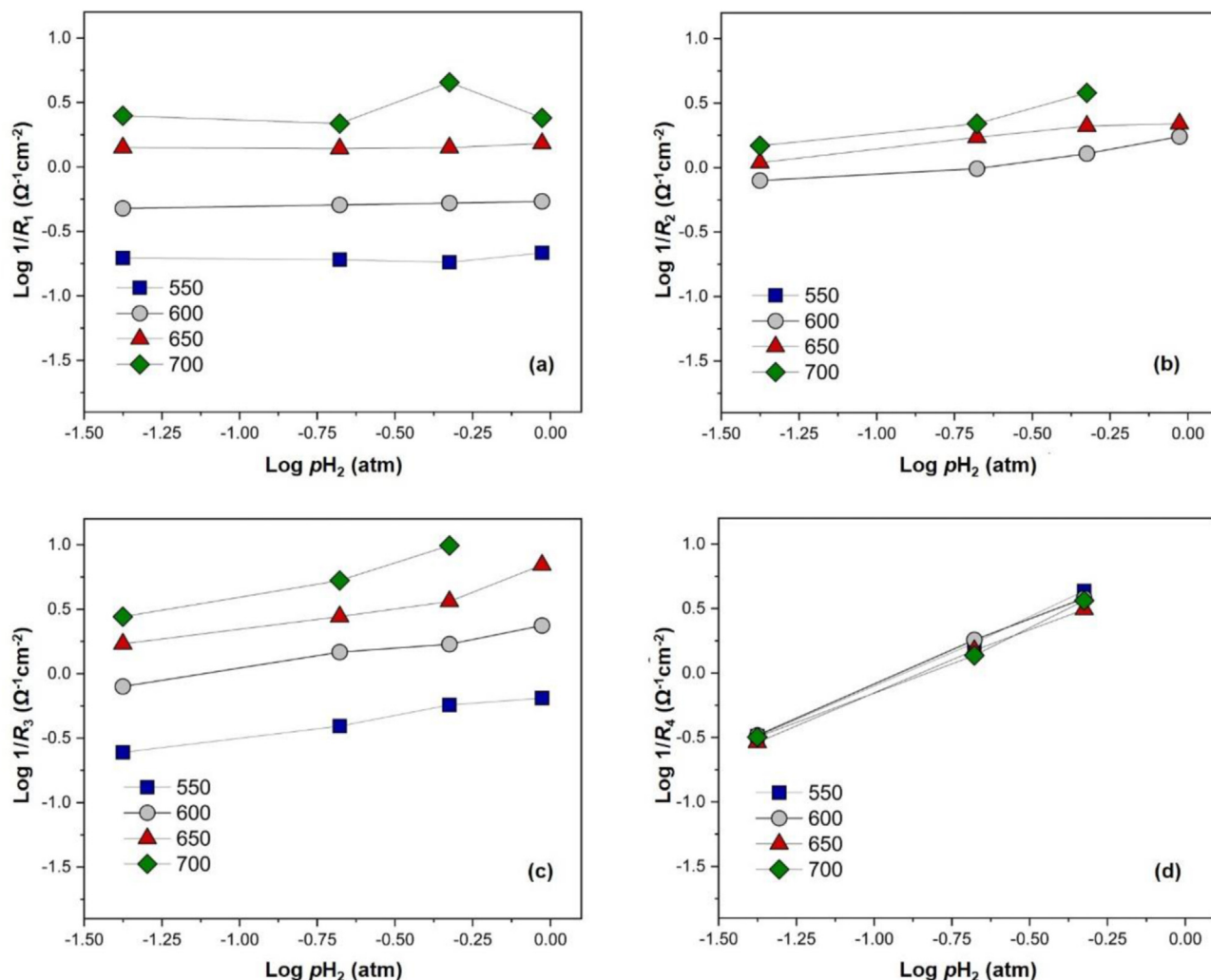


**Fig. 9 –** The pH<sub>2</sub> dependency of 1/R<sub>1</sub>, (b) 1/R<sub>2</sub> (c) 1/R<sub>3</sub> (d) 1/R<sub>4</sub> in the inner chamber, while keeping pH<sub>2</sub> in the outer chamber at 0.05 bar in the temperature range from 550 to 700 °C.

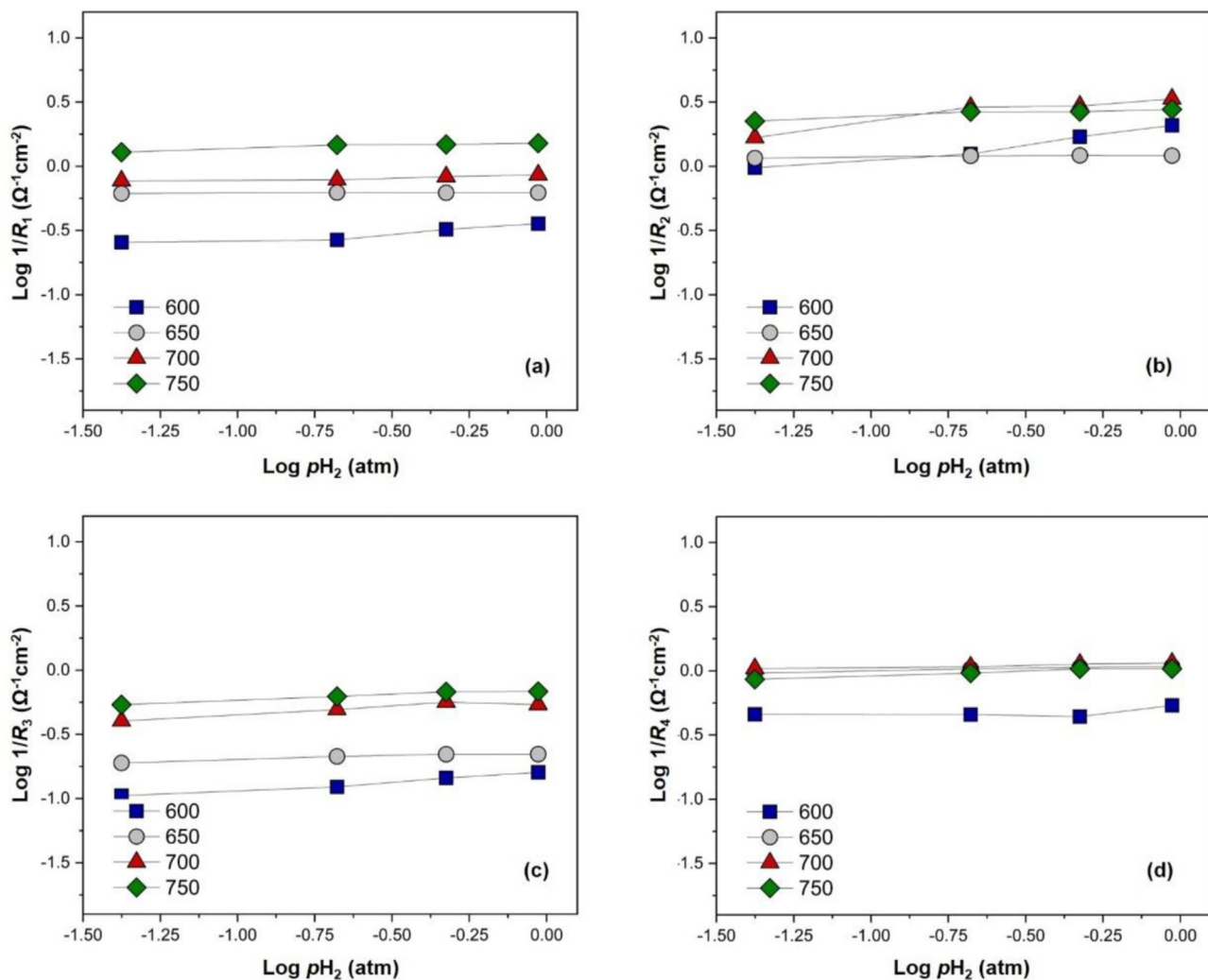


Fig. 10 – The dependency of each polarisation resistance (a)  $1/R_1$ , (b)  $1/R_2$  (c)  $1/R_3$  (d)  $1/R_4$  on  $p\text{H}_2$  in the outer chamber, while keeping  $p\text{H}_2$  in the inner chamber at 0.06 bar in the temperature range from 550 to 700 °C.

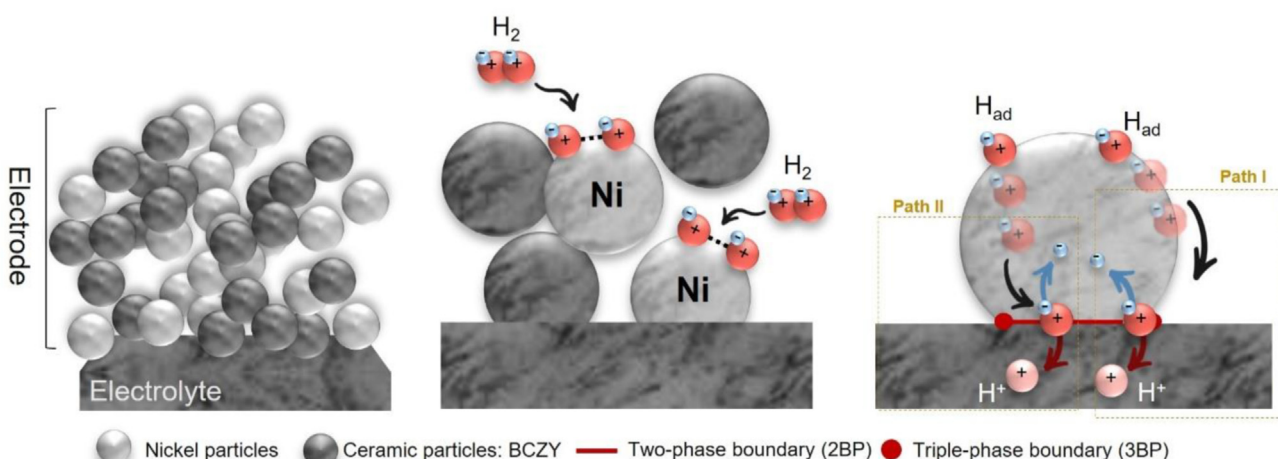


Fig. 11 – Schematic illustration of suggested reaction paths at the electrode in the anodic direction of hydrogen dissociation.

**Table 1 – List of processes proposed (cathodic ↔ anodic).**

|   |   | Process description  | Parameter                                   |
|---|---|--|---|
| a | $H_{(gas)}$ diffusion                     | Gas phase diffusion  | $D_{H_2(gas)}(\text{cm}^2\text{s}^{-1})$    |
| b | $H_{(gas)} \leftrightarrow 2H$            | Dissociative chemisorption   | $k_{chd}(\text{molcm}^{-2}\text{s}^{-1})$   |
| c | I. $H \leftrightarrow H_{Ni\ surface}$    | Hydrogen surface diffusion on Ni   | $D_{H(Ni(surf))}(\text{cm}^2\text{s}^{-1})$ |
|   | II. $H \leftrightarrow H_{Ni\ bulk}$      | Hydrogen bulk diffusion in Ni  | $D_{H(Ni(bulk))}(\text{cm}^2\text{s}^{-1})$ |
| d | $H \leftrightarrow H_{interface}^+ + e^-$ | Redox charge transfer  | $k_{ct}(\text{molcm}^{-2}\text{s}^{-1})$    |
| e | $H_{sc}^+$ migration                      | Proton migration through space charge layer of electrolyte adjacent to the electrode | $R_{H+sc}(\text{ohm cm}^2)$                 |
| f | $H_{electrolyte}^+$ migration             | Proton migration into the bulk of the electrolyte                                    | $\sigma_{H^+}(\text{S cm}^{-1})$            |

boundary capacitances are expected in the order of  $10^{-9} \text{ F cm}^{-2}$  [31] which is three orders of magnitude lower than the value in this work ( $1 - 8 \cdot 10^{-6} \text{ F cm}^{-2}$ ). We thus argue that this high frequency response originates from the proton transport across the space-charge region of the electrolyte bulk adjacent to the Ni electrode (Process e in Table 1) which has been suggested for Ni electrodes on oxide ion conductors [24] and more recently on proton ceramics [36]. The absence of  $pH_2$  dependency for  $1/R_1$  is reminiscent of other reports on SOFC cermet anodes [24,26], where the high frequency semicircle is ascribed to transport phenomena within the cermet composite. Nasani et al. [25] observed that the resistance from a high frequency process decreased significantly with increasing porosity. Similarly, we have observed in this study that the value of  $R_1$  decreases drastically during reduction of the NiO in the cermet electrodes (Fig. 12), believed to reflect increased porosity and contact area between metallic Ni and the electrolyte [37,38]. The microstructure that affects the impedance from this process is presumably sensitive to parameters such as fabrication protocols and materials compositions [39,40].

#### Medium frequency electrode response

The medium frequency response shows a hydrogen dependency of  $1/R_2 \propto pH_2^{(0.15-0.2)}$  on both inner and outer sides.  $1/R_2$  has an average activation energy of 0.52 eV at different

$pH_2$ . The capacitance is calculated in the range  $2-8 \cdot 10^{-4} \text{ F cm}^{-2}$ , which is slightly lower than the reported values [19,41]. It is thus suggested that the medium frequency electrode response may be related to the hydrogen redox charge transfer reaction (process d in Table 1). The hydrogen dependency for process d can be examined using the approach adopted by Nasani et al. [25,42,43]. The associated rate equation for this step is as follows:

$$r_d = k_d a_H \exp\left(-\frac{FE}{2RT}\right) - k'_d a_{H_{electrolyte}^+} \exp\left(\frac{FE}{2RT}\right) \quad (2)$$

where the symmetry coefficient is assumed to be 1/2. The  $k_d$  and  $k'_d$  are the rate constants for the forward and reverse reactions, respectively,  $a_i$  is the activity of species, E is the Nernst electrode potential. By substituting activity coefficients in equation (2), the reaction order of  $pH_2$  is calculated to be 0.25 [25], which is similar to our observations for  $1/R_2$ . It is thus concluded in this work that this medium frequency electrode response is ascribed to the hydrogen redox charge transfer (process d). It is active and limiting on both electrodes, and since we vary  $pH_2$  on only one side at the time, the overall  $pH_2$  dependency is expectedly lower than the theoretical, as observed.

#### Low frequency electrode response

For the low frequency response, the capacitance value ( $C_3$ ) is around  $\sim 8 \cdot 10^{-3} \text{ F cm}^{-2}$ , suggesting that this process may be related to a reaction with considerable chemical capacitance [19,41]. The activation energy of  $R_3$  is calculated to be 1.15 eV. In addition,  $1/R_3$  shows a  $pH_2, \text{inner}^{0.38}$  dependency in Fig. 9c while almost no  $pH_2$  dependency is observed in the outer chamber,  $(1/R_3 \propto pH_{2,outer}^{0.06}$ , in Fig. 10c), suggesting that this impedance is dominated by the inner electrode. There are three electrochemical processes potentially being related to this response. For instance, hydrogen atoms diffuse over Ni surfaces with an activation energy of 0.16–0.4 eV [44]; hydrogen atoms diffuse in the Ni bulk with an activation energy around 1.0 eV [45]; the dissociative adsorption of hydrogen molecules on Ni has an energy of 0.1 eV [46]. The high activation energy of  $R_3$  obtained in this work hence suggests that the electrochemical process is rate-limited by diffusion of hydrogen atoms in Ni bulk. This is contradictory to previous assumptions that the 3 PB is the main charge transfer active site, being rate-limited by surface diffusion [36]. It is thus reasonable to assume that the 2-dimensional 2 PB area is the main charge transfer site instead of the comparatively small 1-dimensional 3 PB line. This argument is

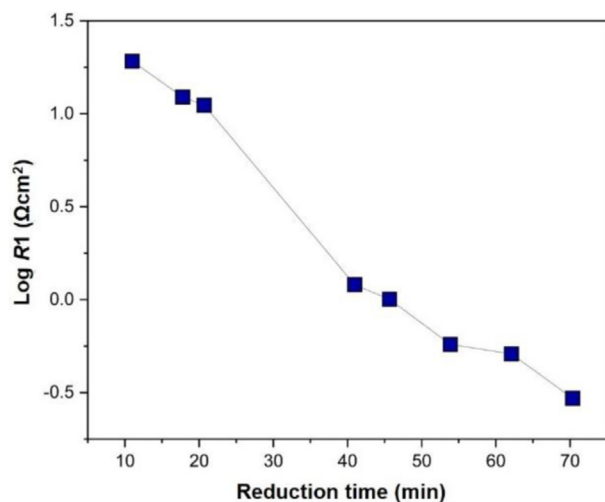


**Fig. 12 – High frequency polarisation resistance  $R_1$  during reduction under pure hydrogen of a Ni-BZCY/BZCY/Ni-BZCY tubular cell at 750 °C.**

**Table 2 – Summary of the characteristics of Ni-BZCY/BZCY/Ni-BZCY tubular cell and their corresponding electrochemical processes.**

| Arc | $f_{\max}$ (Hz) | C ( $\text{Fcm}^{-2}$ )               | $pH_{2,\text{inner}}^x$ | $pH_{2,\text{outer}}^y$ | $E_a$ (eV) | Characteristics   | Process   |
|-----|-----------------|---------------------------------------|-------------------------|-------------------------|------------|---|---|
| 1   | ~10000          | $8 \cdot 10^{-6}$ - $1 \cdot 10^{-6}$ | 0.02                    | 0.05–0.1                | 1.18       | Weak dependence on hydrogen composition on both electrodes.     | Migration of protons (Process e)                        |
| 2   | ~500            | $8 \cdot 10^{-4}$ - $2 \cdot 10^{-4}$ | 0.21                    | 0.15                    | 0.52       | Presence in both electrodes. Relatively sensitive to $pH_2$ .   | $\text{H}/\text{H}^+$ redox charge transfer (Process d) |
| 3   | ~30             | $8 \cdot 10^{-3}$ - $1 \cdot 10^{-3}$ | 0.38                    | 0.06                    | 1.15       | Essential for hydrogen redox mechanism. High activation energy. | Diffusion of atomic hydrogen in Ni bulk (Process c.II)  |
| 4   | ~0.1            | 1–15                                  | 1.04                    | 0.07                    | 0          | Strong dependency of $pH_2$ .                                   | Hydrogen gas diffusion (Process a)                      |

\*The analysis and results presented above are representative for a number of tubular samples.

further supported by the  $pH_2$  dependency that for diffusion of hydrogen atoms (process c.II in Table 1) should be 0.5 [23], being close to 0.38 in this work. We tentatively assign the dominance of the inner electrode to its coarser (more sintered) Ni microstructure.

One may ask why the process chooses a path with such a high activation energy, but as said before, it is a matter of geometry: When the frequency gets this low, in fact close to DC, the process has to go through all steps of the electrochemical reaction at the same rate. While bulk diffusion has a higher activation energy and hence lower transport coefficient, it takes advantage of the 3D diffusion of bulk over the 2D diffusion on the surface and, even more so, the 2D interface for charge transfer of the 2 PB over the 1D interface of the 3 PB. Since this explanation may be considered novel in solid-state electrochemistry, it deserves further mathematical and experimental verification in future studies.

#### Very low frequency electrode response

A strong  $pH_2$  dependence of the polarisation resistance  $1/R_4$  has been only observed by varying  $pH_2$  in the inner chamber ( $1/R_4 \propto pH_{2,\text{inner}}^{1.04}$ ). The capacitance values of  $C_4$  are calculated to be in the range of 1–15  $\text{Fcm}^{-2}$  and they increase at higher  $pH_2$  (Fig. 5). Based on previous reports, this low frequency response can be attributed to a gas diffusion process [35,39,47–49]. The dependency of the capacitance on  $pH_2$  reflects the volume concentration of the hydrogen in the gas phase, which offers chemical capacitive storage by building up or depleting locally as hydrogen molecules diffuse [50].

## Conclusions

In this work, electrochemical impedance spectroscopy has been employed to study the polarisation behaviour of a tubular cell with proton conducting BZCY electrolyte and two asymmetric Ni-BCZY cermet electrodes. The electrochemical characteristics of this tubular cell are summarized in Table 2. Our results have clearly shown that the electrode polarisation resistance is dominated by the inner more sintered and much thicker electrode for all other processes except for the  $\text{H}/\text{H}^+$  charge transfer at the Ni-BZCY interface under experimental conditions in this work. The lowest-frequency

(high capacitance) impedance of the inner electrode shows a strong dependence of  $pH_2$ , ascribed to hydrogen gas diffusion limitation in the thick porous cermet. The high frequency electrode polarisation response shows a weak  $pH_2$  dependency but a strong dependency on microstructure and is assigned to proton transfer across the space charge layer adjacent to the Ni electrode. Impedances at intermediate frequencies have capacitances and  $pH_2$ -dependences that make us assign them to  $\text{H}/\text{H}^+$  charge transfer at the Ni-BZCY interface and atomic hydrogen diffusion in bulk Ni. The presented work contributes to a comprehensive impedance analysis of complete electrochemical tubular cells, yielding a solid fundament for further studies where DC currents are imposed in operation.

## Declaration of competing interest

The authors declare that they have no known competing financial interests or personal relationships that could have appeared to influence the work reported in this paper.

## Acknowledgment

The authors acknowledge funding from the Research Council of Norway NANO2021 project DYNAPRO grant 296548.

## REFERENCES

- [1] Malerød-Fjeld H, Clark D, Yuste-Tirados I, Zanón R, Catalán-Martínez D, Beeaff D, et al. Thermo-electrochemical production of compressed hydrogen from methane with near-zero energy loss. Nat Energy 2017;2:923–31.
- [2] Vøllestad E, Strandbakke R, Tarach M, Catalán-Martínez D, Fontaine M-L, Beeaff D, et al. Mixed proton and electron conducting double perovskite anodes for stable and efficient tubular proton ceramic electrolyzers. Nat Mater 2019;18:752–9.
- [3] Lei L, Zhang J, Guan R, Liu J, Chen F, Tao Z. Energy storage and hydrogen production by proton conducting solid oxide electrolysis cells with a novel heterogeneous design. Energy Convers Manag 2020;218:113044.

- [4] Clark D, Målerød-Fjeld H, Budd M, Yuste-Tirados I, Beeaff D, Aamodt S, et al. Single-step hydrogen production from NH<sub>3</sub>, CH<sub>4</sub>, and biogas in stacked proton ceramic reactors. *Science* 2022;376:390–3.
- [5] Duan C, Kee R, Zhu H, Sullivan N, Zhu L, Bian L, et al. Highly efficient reversible protonic ceramic electrochemical cells for power generation and fuel production. *Nat Energy* 2019;4:230–40.
- [6] Ding H, Wu W, Jiang C, Ding Y, Bian W, Hu B, et al. Self-sustainable protonic ceramic electrochemical cells using a triple conducting electrode for hydrogen and power production. *Nat Commun* 2020;11:1907.
- [7] McIntosh S, Gorte RJ. Direct hydrocarbon solid oxide fuel cells. *Chemical reviews* 2004;104:4845–66.
- [8] Ge XM, Chan SH, Liu QL, Sun Q. Solid oxide fuel cell anode materials for direct hydrocarbon utilization. *Adv Energy Mater* 2012;2:1156–81.
- [9] Duan C, Tong J, Shang M, Nikodemski S, Sanders M, Ricote S, et al. Readily processed protonic ceramic fuel cells with high performance at low temperatures. *Science* 2015;349:1321–6.
- [10] Fabbri E, Pergolesi D, Traversa E. Materials challenges toward proton-conducting oxide fuel cells: a critical review. *Chem Soc Rev* 2010;39:4355–69.
- [11] Malavasi L, Fisher CA, Islam MS. Oxide-ion and proton conducting electrolyte materials for clean energy applications: structural and mechanistic features. *Chem Soc Rev* 2010;39:4370–87.
- [12] Duan C, Kee RJ, Zhu H, Karakaya C, Chen Y, Ricote S, et al. Highly durable, coking and sulfur tolerant, fuel-flexible protonic ceramic fuel cells. *Nature* 2018;557:217–22.
- [13] Zhang H, Zhou Y, Pei K, Pan Y, Xu K, Ding Y, et al. An efficient and durable anode for ammonia protonic ceramic fuel cells. *Energy Environ Sci* 2022;15:287–95.
- [14] Pan Y, Zhang H, Xu K, Zhou Y, Zhao B, Yuan W, et al. A high-performance and durable direct NH<sub>3</sub> tubular protonic ceramic fuel cell integrated with an internal catalyst layer. *Applied Catalysis B: Environmental*. 2022;121071.
- [15] Strandbakke R, Dyrlie O, Hage FS, Norby T. Reaction kinetics of protons and oxide ions in LSM/lanthanum tungstate cathodes with Pt nanoparticle activation. *J Electrochem Soc* 2016;163:F507.
- [16] Ricote S, Bonanos N, Lenrick F, Wallenberg R. LaCoO<sub>3</sub>: promising cathode material for protonic ceramic fuel cells based on a BaCeO<sub>0.2</sub>ZrO<sub>0.7</sub>Y<sub>0.1</sub>O<sub>3–δ</sub> electrolyte. *J Power Sources* 2012;218:313–9.
- [17] Mauvy F, Lalanne C, Bassat J-M, Grenier J-C, Zhao H, Huo L, et al. Electrode properties of Ln<sub>2</sub>NiO<sub>4+δ</sub> (Ln= La, Nd, Pr): AC impedance and DC polarization studies. *J Electrochem Soc* 2006;153:A1547.
- [18] Mogensen M, Lindegaard T. The kinetics of hydrogen oxidation on a Ni-YSZ SOFC electrode at 1000 C. *ECS Proc Vol* 1993;1993:484.
- [19] Bi L, Fabbri E, Sun Z, Traversa E. BaZrO<sub>0.8</sub>Y<sub>0.2</sub>O<sub>3–δ</sub>-NiO composite anodic powders for proton-conducting SOFCs prepared by a combustion method. *J Electrochem Soc* 2011;158:B797.
- [20] Gan Y, Zhang J, Li Y, Li S, Xie K, Irvine JT. Composite oxygen electrode based on LSCM for steam electrolysis in a proton conducting solid oxide electrolyzer. *J Electrochem Soc* 2012;159:F763.
- [21] Strandbakke R, Cherepanov VA, Zuev AY, Tsvetkov DS, Argirisus C, Sourkouni G, et al. Gd-and Pr-based double perovskite cobaltites as oxygen electrodes for proton ceramic fuel cells and electrolyser cells. *Solid State Ionics* 2015;278:120–32.
- [22] Wang S, Zhang J, Gharbi O, Vivier V, Gao M, Orazem ME. Electrochemical impedance spectroscopy. *Nat Rev Methods Prim* 2021;1:41.
- [23] He F, Wu T, Peng R, Xia C. Cathode reaction models and performance analysis of Sm0.5Sr0.5CoO<sub>3–δ</sub>-BaCeO<sub>0.8</sub>Sm0.2O<sub>3–δ</sub> composite cathode for solid oxide fuel cells with proton conducting electrolyte. *J Power Sources* 2009;194:263–8.
- [24] Primdahl S, Mogensen M. Oxidation of hydrogen on Ni/yttria-stabilized zirconia cermet anodes. *J Electrochem Soc* 1997;144:3409.
- [25] Nasani N, Ramasamy D, Brandão AD, Yaremchenko AA, Fagg DP. The impact of porosity, pH<sub>2</sub> and pH<sub>2</sub>O on the polarisation resistance of NiBaZrO<sub>0.85</sub>Y<sub>0.15</sub>O<sub>3–δ</sub> cermet anodes for Protonic Ceramic Fuel Cells (PCFCs). *Int J Hydrogen Energy* 2014;30: e1–.
- [26] Jørgensen MJ, Mogensen M. Impedance of solid oxide fuel cell LSM/YSZ composite cathodes. *J Electrochem Soc* 2001;148:A433.
- [27] Jensen SH, Hauch A, Hendriksen PV, Mogensen M, Bonanos N, Jacobsen T. A method to separate process contributions in impedance spectra by variation of test conditions. *J Electrochem Soc* 2007;154:B1325.
- [28] Bujalski W, Dikwal CM, Kendall K. Cycling of three solid oxide fuel cell types. *J Power Sources* 2007;171:96–100.
- [29] Morejudo SH, Zanón R, Escolástico S, Yuste-Tirados I, Målerød-Fjeld H, Vestre PK, et al. Direct conversion of methane to aromatics in a catalytic co-ionic membrane reactor. *Science* 2016;353:563–6.
- [30] Pergolesi D, Fabbri E, D'Epifanio A, Di Bartolomeo E, Tebano A, Sanna S, et al. High proton conduction in grain-boundary-free yttrium-doped barium zirconate films grown by pulsed laser deposition. *Nat Mater* 2010;9:846–52.
- [31] Xu X, Bi L, Zhao X. Highly-conductive proton-conducting electrolyte membranes with a low sintering temperature for solid oxide fuel cells. *J Membr Sci* 2018;558:17–25.
- [32] Bausa N, Escolástico S, Serra JM. Direct CO<sub>2</sub> conversion to syngas in a BaCeO<sub>0.2</sub>ZrO<sub>0.7</sub>Y<sub>0.1</sub>O<sub>3–δ</sub>-based proton-conducting electrolysis cell. *J CO<sub>2</sub> Util* 2019;34:231–8.
- [33] Mogensen M, Skaarup S. Kinetic and geometric aspects of solid oxide fuel cell electrodes. *Solid State Ionics* 1996;86:1151–60.
- [34] Robinson S, Kjølseth C, Norby T. Comparison of Cu and Pt point-contact electrodes on proton conducting BaZrO<sub>0.7</sub>CeO<sub>0.2</sub>Y<sub>0.1</sub>O<sub>3–δ</sub>. *Solid State Ionics* 2017;306:38–47.
- [35] Murray EP, Tsai T, Barnett SA. Oxygen transfer processes in (La, Sr) MnO<sub>3</sub>/Y<sub>2</sub>O<sub>3</sub>-stabilized ZrO<sub>2</sub> cathodes: an impedance spectroscopy study. *Solid State Ionics* 1998;110:235–43.
- [36] Chen M, Xie X, Guo J, Chen D, Xu Q. Space charge layer effect at the platinum anode/BaZrO<sub>0.9</sub>Y<sub>0.1</sub>O<sub>3–δ</sub> electrolyte interface in proton ceramic fuel cells. *J Mater Chem* 2020;8:12566–75.
- [37] Robinson S, Manerbino A, Grover Coors W, Sullivan N. Fabrication and performance of tubular, electrode-supported BaCeO<sub>0.2</sub>ZrO<sub>0.7</sub>Y<sub>0.1</sub>O<sub>3–δ</sub> fuel cells. *Fuel Cell* 2013;13:584–91.
- [38] Coors WG, Manerbino A. Characterization of composite cermet with 68 wt.% NiO and BaCeO<sub>0.2</sub>ZrO<sub>0.7</sub>Y<sub>0.1</sub>O<sub>3–δ</sub>. *J Membr Sci* 2011;376:50–5.
- [39] Mitterdorfer A, Gauckler L. La<sub>2</sub>Zr<sub>2</sub>O<sub>7</sub> formation and oxygen reduction kinetics of the La<sub>0.85</sub>Sr<sub>0.15</sub>Mn<sub>y</sub>O<sub>3</sub>, O<sub>2</sub>(g) YSZ system. *Solid State Ionics* 1998;111:185–218.
- [40] Sunde S. Monte Carlo simulations of polarization resistance of composite electrodes for solid oxide fuel cells. *J Electrochem Soc* 1996;143:1930.
- [41] Kek D, Bonanos N, Mogensen M, Pejovnik S. Effect of electrode material on the oxidation of H<sub>2</sub> at the metal-SrO<sub>0.995</sub>CeO<sub>0.95</sub>Y<sub>0.05</sub>O<sub>2</sub> 970 interface. *Solid State Ionics* 2000;131:249–59.
- [42] Tsipis EV, Kharton VV. Electrode materials and reaction mechanisms in solid oxide fuel cells: a brief review. *J Solid State Electrochem* 2008;12:1367–91.

- [43] Tsipis EV, Kharton VV. Electrode materials and reaction mechanisms in solid oxide fuel cells: a brief review. III. Recent trends and selected methodological aspects. *J Solid State Electrochem* 2011;15:1007–40.
- [44] Bhatia B, Sholl DS. Chemisorption and diffusion of hydrogen on surface and subsurface sites of flat and stepped nickel surfaces. *J Chem Phys* 2005;122:204707.
- [45] Wang Y, Connétable D, Tanguy D. Hydrogen influence on diffusion in nickel from first-principles calculations. *Phys Rev B* 2015;91:094106.
- [46] He Y, Wang W. H<sub>2</sub> dissociation on H-Precovered Ni (100) surface: physisorbed state and coverage dependence. *J Phys Chem C* 2019;123:5365–77.
- [47] Bennov S. Risoe publication activities in 1998. Risoe National Lab.; 1999.
- [48] Tsuneyoshi K, Mori K, Sawata A, Mizusaki J, Tagawa H. Kinetic studies on the reaction at the La0. 6Ca0. 4MnO<sub>3</sub>/YSZ interface, as an SOFC air electrode. *Solid State Ionics* 1989;35:263–8.
- [49] Østergård M, Mogensen M. Ac Impedance study of the oxygen reduction mechanism on La1–xSr<sub>x</sub>MnO<sub>3</sub> in solid oxide fuel cells. *Electrochim Acta* 1993;38:2015–20.
- [50] Bessler WG. Gas concentration impedance of solid oxide fuel cell anodes: I. Stagnation point flow geometry. *J Electrochem Soc* 2006;153:A1492.